SHORT COMMUNICATION - SPECIAL ISSUE

Preliminary evidence on laboratory experiments to detect the impact of transient flow on bedload transport

Łukasz Przyborowski[1] · Michael Nones[1] · Magdalena Mrokowska[1] · Leszek Książek[2] · Cong Ngoc Phan[2,3] · Andrzej Strużyński[2] · Maciej Wyrębek[2] · Bartosz Mitka[2] · Szymon Wojak[2]

Abstract
Trapezoidal-shaped hydrographs are typical of anthropized rivers, as this form is generally associated with the release of water from hydropower dams. To investigate how such unnatural waves can affect bedload rate, preliminary flume experiments were performed in Krakow, Poland, looking at bedload transport rate, bed shear stress and bed morphology. In addition, close-range bed surface photogrammetry was used to investigate bed changes due to the passage of the flood wave. Three scenarios, having the same water volume but different wave magnitudes, were tested. The lowest wave showed almost no sediment transport and no visible changes in bed morphology, while higher waves changed the bed morphology, creating erosion and accumulation zones. The highest wave was characterized by an 8-shaped hysteresis of the bedload rate with a peak during the wave maximum. The lag time between the maximum bedload rate and the wave plateau was longer than expected due to zero-slope conditions.

Keywords Acoustic Doppler velocimeter · Bedload · Unsteady flow · Laboratory studies · Velocity measurements · Digital close-range photogrammetry

Abbreviations

ADV U_P	Mean streamwise velocity for wave plateau measured by ADV (m s^{-1})
ADV u_{*p}	Mean bed shear velocity extrapolated from ADV records for wave plateau (m s^{-1})
ADV W_P	Mean vertical velocity measured by ADV probe during the wave plateau (m s^{-1})
B	Flume width (m)
$B\,D_{xx}$	Particle diameter for sediment gathered from the bed after test (mm)
C	Wave celerity (m s^{-1})
CP	Control point
ChP	Check point
D_{50}	Median diameter of sediment particles (mm)
e	Kinetic energy (m)
GCP	Ground control point

✉ Łukasz Przyborowski
lprzyborowski@igf.edu.pl

Michael Nones
mnones@igf.edu.pl

Magdalena Mrokowska
m.mrokowska@igf.edu.pl

Leszek Książek
leszek.ksiazek@urk.edu.pl

Cong Ngoc Phan
phancongngoc1402@gmail.com

Andrzej Strużyński
rmstruzy@cyf-kr.edu.pl

Maciej Wyrębek
m.wyrebek@gmail.com

Bartosz Mitka
bartosz.mitka@urk.edu.pl

Szymon Wojak
szymon.wojak@wp.pl

1   Department of Hydrology and Hydrodynamics, Institute of Geophysics Polish Academy of Sciences, Warsaw, Poland

2   Faculty of Environmental Engineering and Land Surveying, University of Agriculture in Kraków, Kraków, Poland

3   Institute of Chemistry, Biology and Environment, Vinh University, Vinh, Vietnam

Springer

GSD	Ground sample distance (m)
G	Gravitational acceleration (m s^{-2})
H	Water depth (m)
H_b	Depth of the base flow (m)
H_p	Depth of the peak flow (m)
$I\,D_{xx}$	Particle diameter by mass for sediment gathered from the bed before tests (mm)
L_{1-4}	Distance between the resistive sensors 1 and 4 (m)
M	Cumulative sediment mass (kg)
MHD U_P	Mean streamwise velocity measured by MHD during the wave plateau (m s^{-1})
P_{gt}	Unsteadiness parameter
q	Bedload rate (kg s^{-1})
Q	Discharge (m^3 h^{-1})
Q_P	Discharge during wave plateau (l s^{-1})
Re$_*$	Boundary Reynolds number
Re$_{*p}$	Boundary Reynolds number during wave plateau
S_0	Bed slope
S_w	Hydraulic slope
T_{lag}	Time difference between reaching hydrograph plateau and sedimentograph peak (s)
$T\,D_{xx}$	Particle diameter by mass for sediment gathered from the trap (mm)
u'	Streamwise velocity fluctuation
U_0	Time-averaged streamwise velocity during base flow (m s^{-1})
U_p	Time-averaged peak streamwise velocity during wave plateau (m s^{-1})
u_*	Bed shear velocity (m s^{-1})
$u_{*,0}$	Bed shear velocity of the base flow (m s^{-1})
u_{*p}	Mean shear velocity during wave plateau (m s^{-1})
U	Mean streamwise velocity (m^3 s^{-1})
u'	Vertical velocity fluctuation
W_k	Total flow work index
W_T	Total bedload (kg)
W_{T*}	Dimensionless total bedload
Vol	Total volume of water under the hydrograph (m^3)
Z	Distance of the ADV measuring point from the bed (m)
α	Saint-Venant coefficient
ρ	Water density (kg m^{-3})
ρ_s	Sediment density (kg m^{-3})
Λ	Wavelength (m)
$\tau_{adv,p}$	Reynolds stress calculated from ADV records for the plateau (N m^{-2})
τ_*	Shields parameter
$\tau_{*,p}$	Shields parameter during the wave plateau
τ_b	Bed shear stress (N m^{-2})

$\tau_{b,}$	Bed shear stress during the wave plateau (N m^{-2})
$\tau_{BedAdv,p}$	Bed shear stress for the wave plateau extrapolated from τ_{adv} (N m^{-2})
$\tau_{BedAdv,r}$	Bed shear stress for the wave rising limb extrapolated from τ_{adv} (N m^{-2})
τ_{SV}	Instantaneous bed shear stress (N m^{-2})
η	Hydrograph asymmetry
ν	Kinematic fluid viscosity (m^2 s^{-1})
Γ_{HG}	Unsteadiness parameter
ω	Stream power (N m^{-1} s^{-1})
ΔH	Change of the flow depth between peak and base flow (m)
Δt	Duration (s)
ΔT	Wave duration (s)
ΔT_R	Durations of rising limb (s)
ΔT_P	Durations of wave plateau (s)
ΔT_F	Duration of falling limb (s)
ΔT_{SP}	Time to peak rate of sedimentograph (s)

Introduction

The large part of sediment transported by streams, and the associated changes to the bed surface composition, occurs during natural flooding events (e.g. Berta and Bianco 2010; Lee and Balachandar 2012; Michalik and Książek 2009), hydropower operations (Aigner et al. 2017), and dam-break events (Abderrezzak et al. 2008). These high-magnitude, unsteady flows can first mobilize and then transport large quantities of bed sediments. Consequently, the sediment transport phenomenon shapes the morphology of the riverbed, which is a key factor for the water flow conditions at low water stages, influencing the environmental flow (Książek et al. 2019) and creating a mosaic of habitats for aquatic organisms (Książek et al. 2020). What is more, flooding events are also responsible for the remobilization of pollutants entrapped in the bed (Hitchcock 2020).

Nowadays, a large part of rivers worldwide is regulated by hydraulic infrastructures (e.g. dams or weirs), affecting not only the longitudinal connectivity and preventing sediments from freely moving from the upstream basin towards the river mouth (Bracken et al. 2015), but also changing the hydraulic conditions because of backwater effects (Bartnik et al. 2005; Maselli et al. 2020). The presence of in-channel hydraulic infrastructures or natural obstructions can eventually result in downstream bed degradation and/or variation to the grain size composition of the surficial bed coverage, especially in the case of large flooding events or managed flow releases (Luo et al. 2012; Nones et al. 2019). However, these outcomes derive from studies generally performed assuming steady-state conditions, which represents an oversimplification in representing natural systems driven by

transient hydrology. The transience of natural hydrographs and dam-break flows presents a barrier to applying the mechanistic understanding of sediment transport dynamics developed under steady flows in laboratory experiments to natural rivers.

At timescales of single flooding events (from the initiation of motion to the cessation of bed material transport) to timescales of multiple flood waves, it remains an open question how steady and transient flows differ in terms of their effects on bed channel morphology and bedload sediment dynamics. Therefore, additional studies are needed to distinguish between phenomena that occur under steady flow and those that require a transient hydrograph (Mrokowska et al. 2018; Phillips et al. 2018; Mrokowska and Rowiński 2019).

Numerous experimental studies on transient flow explore the role of magnitude and duration of a single flood wave (Bombar et al. 2011; Guney et al. 2013; Humphries et al. 2012; Li et al. 2018; Mao 2012; Wang et al. 2021) or a single hydrograph cycle (Phillips et al. 2018; Plumb et al. 2020) on the total bedload transport and development of bed surface texture in unimodal or bimodal sediment beds. A growing number of experimental studies provide data on the bedload rate q versus flow rate Q relationship, which is usually affected by a temporal shift in the peaks of variables. As a result, the shape of the $Q(q)$ relation is generally identified in the form of a clockwise or counterclockwise hysteresis (Guney et al. 2013; Mao 2012; Waters and Curran 2015) and the type of hysteresis depends on various factors including initial bed structure, armouring, presence of bedforms and sediment feeding conditions.

Previous experimental studies have demonstrated that flow unsteadiness enhances sediment transport and that the total sediment yield resulting from the passage of a flood wave exceeds sediment yield for the equivalent-volume steady flow (Li et al. 2018; Wang et al. 2015). Other characteristics of the flow such as hydrograph magnitude, volume and shape are among the controls on the sediment yield (Wang et al. 2015; Redolfi et al. 2018). The presence of backwater can also change the predicted yield (Jin et al. 2016; Wu and Nitterour 2020). Nonetheless, factors related to sediment availability including sediment composition, bed structure and sediment supply conditions can also affect the total yield. In the present paper, due to the small number and timescale of the simulated waves, only preliminary data about sediment composition are provided, as the research focus is shifted towards analysing the total sediment yield and changes in bed morphology, without accounting for localized phenomena.

The techniques of close-range photogrammetry can provide universal methods and approaches to the geometric measurement of many objects. As a result, there is a wide range of potential application areas such as architecture, archaeology and cultural heritage, civil engineering, industrial applications, medicine, and many others where it is important to measure the geometry of the objects quickly and precisely (Luhmann et al. 2019). To date, various laboratory approaches have been used to measure the bed elevation before and after the passage of designed unsteady flow, including laser scanning (Waters and Curran 2015), ADV profiling (Wang et al. 2019) and close-range photogrammetry. The latter method, applied in the present work, produces digital surface model (DSM), needed for qualitatively comparing the bed morphology before and after the passage of a flood wave, eventually pointing out bedforms resulting from the local hydrodynamics. Such methods and approaches can be applied to measure many objects, deriving the respective geometry (Luhmann et al. 2019). Indeed, the capability to automatically process images while maintaining sub-pixel accuracy (Mikrut 2009), combined with the increasing availability of large computing, helped in growing the number of applications of digital cameras to produce 3D representations of reality. In practice, two methods are used in parallel to obtain high-quality 3D models of digitized objects: technology based on laser scanners, directly acquiring 3D point clouds, and technology based on creating object geometry based on a set of properly acquired 2D photographs—structure from motion (SfM). Both technologies, under appropriate conditions, allow obtaining the same product with a very similar accuracy (Mitka and Pluta 2016). Usually, the SfM technique is appropriate in the case of a good surface texture, densely overlapping images, and a camera that is either pre-calibrated or at least mechanically stable during image acquisition. The typically achievable accuracy lies in the range of 0.5–2 pixels, depending on the method of feature extraction and the measure of similarity between images (Luhmann et al. 2019).

In the present study, we report results from laboratory flume experiments performed at the Laboratory of Faculty of Environmental Engineering and Land Surveying, University of Agriculture in Kraków, Poland, designed to investigate the effects of flood magnitude and duration on bedload dynamics. After the presentation of the flume set-up and the methods applied, we analysed three sets of experiments, where we imposed singular trapezoidal flood waves as forcing terms, to mobilize a well-mixed bimodal sediment bed. The flood magnitude differed between runs, but the total water volume circulated during the runs and the flume slope remained constant.

Materials and methods

Experimental set-up and procedure

The experiments were performed in a tilting flume (12 m long, 0.485 m wide and 0.60 m deep), located at the

University of Agriculture in Kraków, Poland (Przyborowski et al. 2021). The flume is mainly made of steel, with glass side windows, and the closed-circuit delivers water to the main channel from an upper tank, via an inlet pipe, and regulated by a manually or electronically controlled valve, with an ultrasonic flow meter measuring the flow rate at 10 Hz (Fig. 1). The first 0.25 m of the flume bed was fixed using coarse gravel (i.e. armoured bed in Fig. 1); then, the next 7.5 m was covered with a 12-cm-thick layer of gravel with median grain size diameter $D_{50} = 4.6$ mm. The last part of the flume (1-m-long, non-movable bed in Fig. 1) was made of a smooth plate to ease the delivery of the transported material to the outlet, where a sediment trap is installed. The trap is hanged on an electronic weight, which weights the material at a frequency of 1 Hz, with an accuracy of 0.1 g. Five resistive sensors, mounted 1 cm above the bed along the flume (2.50 m, 3.60 m, 4.64 m, 5.60 m, 6.57 m from the outlet), registered the water level with a frequency of 20 Hz and standard deviation of 0.012 cm. Two velocimeters, namely an acoustic Doppler velocimeter (ADV, Sontek 100 MHz down-looking probe, velocity recording set up at 50 Hz) and a magnetohydrodynamic probe (MHD, velocity recording set up at 16 Hz), were installed in the middle of the flume at 2 and 7 cm above the bed, and at 5.08 and 4.07 m from the flume outlet, respectively. Additionally, a digital camera with a 20 MP resolution was mounted above the flume, which was used for bed photogrammetry.

A series of tests were first performed to determine the water discharge responsible for the initiation of sediment movement (incipient motion conditions). The movement was observed with discharge higher than $Q = 80$ m^3 h^{-1}, equal to 30% of the maximum opening of the inlet valve.

Based on that, three scenarios were chosen for testing: 40%, 50% and 60% of the maximum opening of the inlet valve, corresponding to a maximum discharge of $Q = 114$ m^3 h^{-1}, 151 m^3 h^{-1} and 176 m^3 h^{-1}, and named S, U and V, respectively (Table 1). All the experiments were designed to have a trapezoidal shape of the hydrograph, keeping the wave asymmetry η (Eq. 3) close to 1 and the total water volume Vol flowing into the flume constant (13.2 m^3). Therefore, the duration of the rising and falling limbs of the wave changed according to each scenario. Each scenario was repeated at least three times, but only one from each series with the best hydrograph shape was chosen for further description in this paper. The repetitions that had not been chosen had inconsistent wave duration, so, in these preliminary results, they were omitted for the sake of clarity in comparison.

In detail, the operating conditions were (Δt denotes the duration of each phase):

1. filling of the flume up to the base flow conditions ($Q = 80$ m^3 h^{-1}), for which no sediment movements were observed ($\Delta t = 150$ s);

Fig. 1 Sketch of the tilting flume installed in the hydraulic laboratory of the University of Agriculture in Kraków, Poland (adapted from Mrokowska et al. 2016)
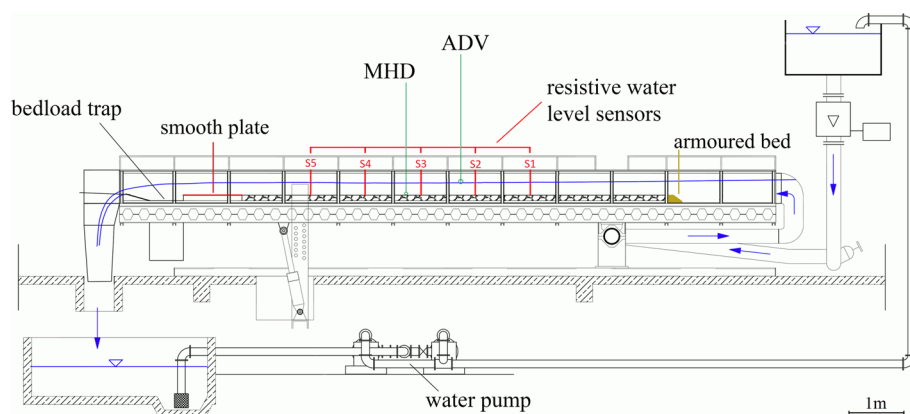
Table 1 Basic hydrograph parameters

Run	Q_p (l s^{-1})	H_b (m)	H_p (m)	ΔT_R (s)	ΔT_P (s)	ΔT_F (s)	ΔT_{SP} (s)	T_{lag} (s)	W_k	Γ_{HG}	η	P_{gt}
S-40%	31.26	0.02	0.096	156	165	158	127	−29	1.70	0.0011	0.98	0.0012
U-50%	41.64	0.02	0.117	148	100	143	181	33	2.59	0.0028	1.03	0.0014
V-60%	49.23	0.02	0.122	117	99	118	141	24	2.72	0.0037	0.99	0.0015

Q_P—discharge during wave plateau; H_b—water depth of base flow; H_p—water depth during wave plateau; ΔT_R—duration of the rising limb of the wave; ΔT_P—duration of the plateau of the wave; ΔT_F—duration of receding limb of the wave; ΔT_{SP}—time to peak rate of sedimentograph; T_{lag}—time difference between reaching the hydrograph plateau and sedimentograph peak ΔT_{SP}—ΔT_R; W_k—total flow work index; Γ_{HG}—unsteadiness parameter; η—hydrograph asymmetry; P_{gt}—ascension unsteadiness parameter

2. stabilization of the base flow ($\Delta t = 120$ s; valve open at 30%; $Q = 80$ m^3 h^{-1});

3. rising limb of the wave (Δt for S scenario $= 156$ s; for $U = 148$ s; for $V = 117$ s);

4. maximum water discharge, wave plateau conditions (for S scenario, $Q = 114$ m^3 h^{-1}, $\Delta t = 165$ s; for U: $Q = 151$ m^3 h^{-1}, $\Delta t = 100$ s; for V, $Q = 176$ m^3 h^{-1}, $\Delta t = 99$ s);

5. falling limb of the wave (Δt for $S = 158$ s; for $U = 143$ s; for $V = 118$ s);

6. stabilization of the base flow ($\Delta t = 120$ s);

7. flume emptying ($\Delta t = 30$ s).

The exact positioning of all the measurement devices was checked before each run, after the sediment levelling. To allow for comparison, the internal devices timers were synchronised by an external source. The devices were turned on in the following order, dictated by the water level requirements: resistive sensors, flow meter, sediment balance, MHD and ADV. During the run, inert ash was manually added at a constant rate to the flume inlet to ensure enough scatter material for acoustic velocimetry.

Flow hydrographs characterization

In the literature, three non-dimensional parameters were generally used to describe triangular and trapezoidal flow hydrographs (Bombar et al. 2011): total flow work index W_k, to describe the magnitude of the water volume acting on the bedload (Yen and Lee 1995), Eq. (1); unsteadiness Γ_{HG}, which shows how flashy is the hydrograph (Graf and Suszka 1985), Eq. (2); and hydrograph asymmetry η (Wang et al. 2015), Eq. (3):

$$W_k = \frac{u_{*,0}^2 \text{Vol}}{gH_b^3 B} \tag{1}$$

$$\Gamma_{HG} = \frac{1}{u_{*,0}} \frac{\Delta H}{\Delta T} \tag{2}$$

$$\eta = \frac{\Delta T_R}{\Delta T_F}, \tag{3}$$

where $u_{*,0}$ represents the bed shear velocity of the base flow condition, Vol is the total volume of water under the hydrograph (excluding the base flow, kept around $2.2 * 10^{-3}$ m^3 s$^{-1} = 80$ m^3 h^{-1}), H_b indicates the base flow depth, B represents the flume width, g is the gravitational acceleration, ΔH indicates the change of the flow depth between peak and base flow (H_p-$\underline{H}_b$), and ΔT represents the hydrograph duration, modified to account for the trapezoidal shape of the hydrograph. Hence, $\Delta T = \Delta T_R + \Delta T_P + \Delta T_F$,

where ΔT_R, ΔT_P and ΔT_F are the durations of rising limb, plateau and falling limb, respectively.

To investigate the effects of a specific wave on bedload transport rates, we compared the unsteadiness of the waves Γ_{HG}, and, for the duration of wave plateau, the stream power:

$$\omega = \tau_{b,p} U, \tag{4}$$

where U is the mean velocity, computed as the discharge at the inlet, divided by the cross-sectional area at the position of the first resistive sensor.

The bed shear stress τ_b is derived from the Saint-Venant model for a diffusive wave:

$$\tau_b = \rho g h S_w, \tag{5}$$

where ρ is the water density, g is the gravitational acceleration, h represents the water depth, and S_w is the water surface slope. The latter was obtained as the difference in energy height (hydraulic slope):

$$S_w = \frac{(h_4 + e_4) - (h_1 + e_1)}{L_{1-4}}, \tag{6}$$

where L_{1-4} is the distance between the resistive sensors 1 and 4, h_1 and h_4 are the water depths in the location of the resistive sensors 1 and 4, respectively. The total head at sensors 1 and 4, e_1, e_4, was computed as the sum of water level and kinetic energy (Eq. 7), assuming a zero-slope bed.

$$e = \frac{\alpha U^2}{2g}, \tag{7}$$

where α is the Saint-Venant coefficient equal to 1.

The parameters for Shields curve, boundary Reynolds number and Shields number were calculated as:

$$\text{Re}_p^* = \frac{D u_*}{v} \tag{8}$$

$$\tau_* = \frac{\tau_b}{(\rho_s - \rho) g D_{50}}, \tag{9}$$

where v is the kinematic fluid viscosity, D_{50} represents the median diameter of sediment, u_* is the bed shear velocity, and ρ_s is the sediment density.

The wave celerity was calculated for the shallow water conditions ($\Delta H/\lambda < 0.05$), where λ is the wavelength (Eq. 10) and C is the wave celerity (Eq. 11).

$$\lambda = \Delta T \sqrt{g \Delta H} \tag{10}$$

$$C = \sqrt{g \Delta H} \tag{11}$$

The velocity measurements were conducted using SonTek 100 MHz down-looking ADV, choosing a sampling frequency of 50 Hz, while the sampling volume was positioned around 2 cm above the bed. Signal-to-noise ratio and correlation thresholds, in addition to 3D space thresholding filter (e.g. Goring and Nikora 2002; Wahl 2003; Parsheh et al. 2010), were used to clean measured velocities from bad records and spikes. Streamwise u' and vertical w' velocity fluctuations were used to calculate shear stresses and, following the method of Manes et al. (2007), to extrapolate it to the bed level and to compute shear velocities. Therefore, the shear velocity was calculated in two ways: using the bed shear stress derived from the water slope and using the shear stress from velocity fluctuations during the plateau extrapolated to the sediment crest level.

$$u_{*,p} = \sqrt{\frac{\tau_{b,p}}{\rho}} \tag{12}$$

$$\text{ADV}u_{*,p} = \sqrt{\frac{\tau_{\text{BedAdv}}}{\rho}}, \tag{13}$$

where τ_{BedAdv} is the value of the bed shear stress extrapolated from Reynolds stress recorded by ADV during the plateau and calculated as:

$$\tau_{\text{BedAdv}} = \frac{\tau_{\text{adv,p}} H_p}{h - z}, \tag{14}$$

with z indicating the distance of the ADV measuring point from the bed.

$$\tau_{\text{adv,p}} = -\rho \overline{u'w'} \tag{15}$$

Using the velocity measurements, there is also available an alternative version of unsteadiness to calculate, based on the concept shown by Bombar et al. (2011). We called this parameter ascension unsteadiness, since it refers to the rising limb of the wave:

$$P_{\text{gt}} = \frac{\left| gS_{\text{o}} - \left(\frac{U_p - U_o}{\Delta T_R} \right) \right|}{g}, \tag{16}$$

where U_p is the peak velocity (time-averaged during plateau), U_o is the baseflow velocity, and S_o is the bed slope. In our case, instead of the bed slope, we used the mean hydraulic slope during the rising limb of the wave, as the flume was not tilted.

Following Bombar et al. (2011), the dimensionless total bedload was calculated as:

$$W_T^* = \frac{W_T}{\rho_s B D_{50}^2}. \tag{17}$$

Digital close-range photogrammetry

Correct preparation and implementation of the overall process of photos acquisition require defining specific resolution of the images and geometry of the photo block, ensuring the appropriate number and geometry of control points, as well as the correct determination of the camera's internal orientation elements. A proper combination of all these parameters results paramount in realizing an accurate DSM of the study area.

The photo sessions were conducted with a photo camera set for native resolution (20 Mpix), following a similar photogrammetry technique proposed by Faezal et al. (2016) and Stojic et al. (1998). The spatial coordinates (X, Y, Z) of 14 ground control points (GCP) were acquired with a Topcon OS-103 total station. A unit of Sony DSC-RX10M4 camera was mounted on a steel bar centrally above the flume width to capture a series of digital images of the channel bed. The distance from the bed has been fixed to 1.4 m. The camera was moved along the longitudinal profile of the flume with a 10-cm interval to capture 64 digital frames of the bed surface. It allowed obtaining longitudinal coverage for photos equal to 90% and average GSD = 0.18 mm (Książek et al. 2021).

The development of the photogrammetric project was performed in Agisoft Metashape Professional software. Ten of the measured GCP were used in the block alignment as control points (CP), and four as checkpoints (ChP) to verify the accuracy of the obtained model (Fig. 2).
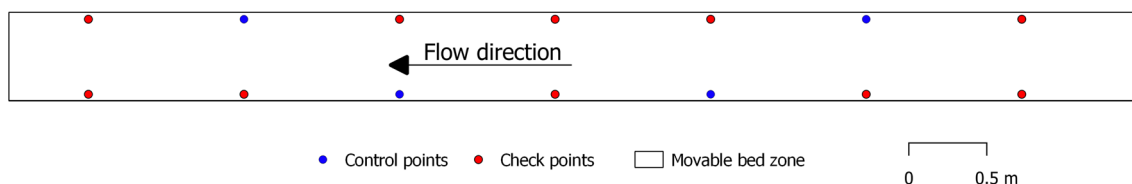

Fig. 2 Arrangement of control points (CP) and checkpoints (ChP) in the photo block

Results

Hydrograph parameters

The hydrograph asymmetry η was close to 1 in each scenario (Table 1). The rate of unsteadiness of the wave characterised by Γ_{HG} varied between cases. In comparison with the lowest wave S, wave U reached 252% of its Γ_{HG} value, while the biggest wave V reached 333%, being the steepest and shortest of all cases (Table 1).

The ascension unsteadiness parameter P_{gt}, as it refers only to the rising limb of the wave, also increased with the wave height, but it had much lower variability than Γ_{HG}. Indeed, there was only a 25% rise between the runs S and V (Table 1).

The flow work index W_k reached the value of 1.7 for run S, while increased by 52% and 60% for the runs U and V, respectively (Table 1).
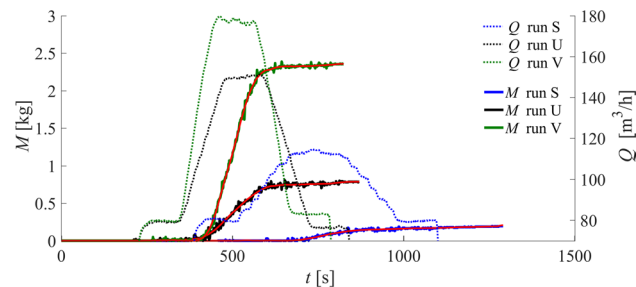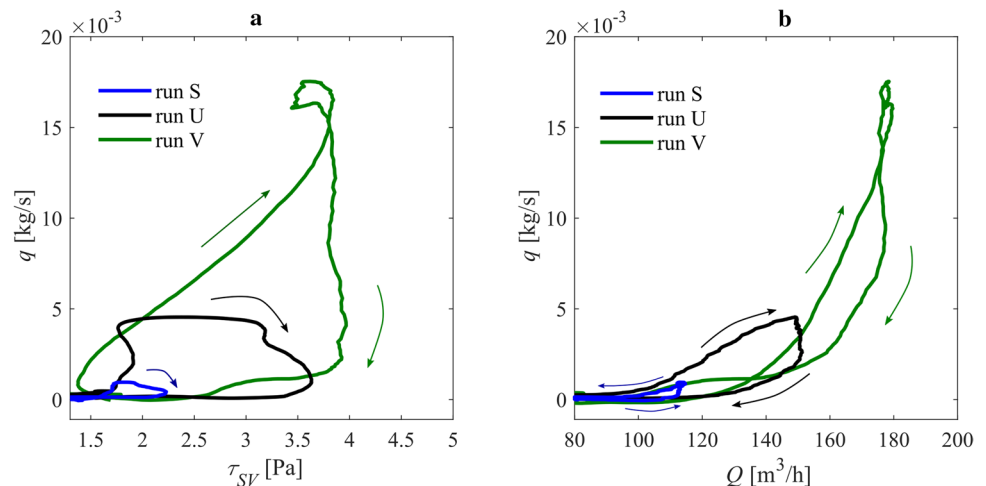
Fig. 3 Cumulative sediment mass, M (values smoothed using Savitzky–Golay filter shown as red lines), during the passage of test hydrographs

Bedload transport

In our experiments, the bedload transport rate is expressed in terms of cumulative sediment mass, M, and the weight of the sediment transported per unit time, q. The cumulative mass measured during the experiments was smoothed using Savitzky–Golay filter (Savitzky and Golay 1964) as in previous studies (Mrokowska et al. 2016, 2018), and measured and processed data are shown in Fig. 3. The smoothed data were then used to evaluate the bedload transport rate as the first derivative of cumulative sediment mass. Further, the time to peak of sedimentograph, ΔT_{SP}, and the lag time between the beginning of the water wave plateau and the sedimentograph peak, T_{lag}, were calculated (Table 1).

Figure 3 shows that, in tests U and V, the sediment transport initiated on the rising limb of the hydrographs, continued along the plateau and then considerably decreased on the falling limb. Run V had the shortest duration of the rising limb, but it had two peaks in sediment transport rate. In the U case, the time to peak of the sedimentograph and the time of the rising limb were proportionally longer (26% and 28% time increase), while the lag time T_{lag} increased by 37% (Table 1).

The bedload transport rate q plotted against the instantaneous bed shear stress τ_{SV}, which is a time series of stress derived from (Eq. 5), shows the increase in both along the rising limb of hydrograph. In the case of run V, the maximum q corresponds with the maximum bed shear stress in the plateau region (Fig. 4a), while in the case of the smaller waves, S and U, the bedload transport rate achieved the peak value before the maximum bed shear stress.

The bedload transport rate q versus flow rate relationship Q (Fig. 4b) takes the form of a clockwise hysteresis for the U run and 8-shaped hysteresis for the V test, with a clear indication of maximum sediment transport along the flow plateau region. For run S, no sediment transport was detected on the wave limbs, and it appeared shortly during

Fig. 4 Relationship between: **a** bedload transport rate q and instantaneous bed shear stress τ_{SV}; **b** bedload transport rate q and flow rate Q, for test hydrographs

the hydrograph plateau, resulting in an anticlockwise hysteretic Q–q relationship (Fig. 4) and negative T_{lag} (Table 1).

The bed shear stress acting on the sediment during the wave plateau $\tau_{b,p}$ (Table 2) for the U wave increased by 68% and for the biggest wave V increased by 95%, in comparison with the smallest wave S. The extrapolation of the results from the ADV measurements showed that $\tau_{BedAdv,p}$ increased by 11% and 51% in comparison with the S run (Table 2). The shear velocity increased by 32% and 42% for runs U and V, respectively, while the ADV extrapolation resulted in a smaller increase in shear velocity—by 5% and 22% for U and V, respectively (Table 2). A time span of 248 s between the beginning of the wave and the end of the plateau

part resulted in 0.70 kg cumulative sediment load in run U, while, for the run V, 216 s moved 2.07 kg of sediment.

The grain size distribution of the bed sediment collected in the trap at the end of the flume revealed that, for the runs S and U, there was an almost identical composition of the transported sediment, with only minimal skew in lower fractions in comparison with the initial conditions (Table 3, Fig. 5). In the case of the highest wave generated in run V, the composition of the transported sediment shifted substantially towards the coarser fractions, as the trap entrapped mostly sediments with a median diameter between 4 and 6.3 mm, while the bed granulometry measured in the middle of the flume did not show such a difference (Table 3, Fig. 5).

Table 2 Shear and sediment transport coefficients

| Run	$\tau_{b,p}(N\,m^{-2})$	$\omega\ (N\,m^{-1}\,s^{-1})$	$u_{*,p}$ (m s^{-1})	ADV $u_{*,p}$ (m s^{-1})	Re$_{*,p}$	$\tau_{BedAdv,p}$ $(N\,m^{-2})$	$\tau_{BedAdv,r}$ $(N\,m^{-2})$	$\tau_{*,P}$	W_T (kg)	W_T^*
S	1.9	1.6	0.043	0.041	152	1.665	1.358	0.033	0.18	6.55
U	3.2	2.7	0.057	0.043	197	1.844	1.466	0.056	0.79	28.75
V	3.7	3.1	0.061	0.050	212	2.524	2.012	0.065	2.36	85.89

$\tau_{b,p}$—mean bed shear stress during the wave plateau; ω—stream power for the wave plateau; $u_{*,p}$—mean shear velocity during the wave plateau; ADV $u_{*,p}$—mean bed shear velocity extrapolated from ADV records; Re$_{*,p}$—boundary Reynolds number during the wave plateau; $\tau_{BedAdv,p}$—bed shear stress for the wave plateau extrapolated from τ_{adv}; $\tau_{BedAdv,r}$—bed shear stress for the wave rising limb extrapolated from τ_{adv}; $\tau_{*,p}$—Shields stress during the wave plateau; W_T—total bedload; W_T^*—dimensionless bedload

Table 3 Grain size composition of the bed material

$I\,D_{16}$ (mm)	$I\,D_{50}$ (mm)	$I\,D_{84}$ (mm)	Run	$T\,D_{16}$ (mm)	$T\,D_{50}$ (mm)	$T\,D_{84}$ (mm)	$B\,D_{16}$ (mm)	$B\,D_{50}$ (mm)	$B\,D_{84}$ (mm)
			S	2.46	3.55	5.37	2.42	3.52	5.29
2.42	3.61	5.42	U	2.45	3.56	5.40	2.42	3.52	5.30
			V	2.19	3.33	4.90	2.41	3.51	5.28

D_{xx}—characteristic diameter of sediment particles; xx—percentage of finer sediment; $I\,D_{xx}$—characteristic particle diameter for sediment gathered from the bed before tests; $T\,D_{xx}$—characteristic particle diameter for sediment gathered from the trap; $B\,D_{xx}$—characteristic particle diameter for sediment gathered from the bed after each test

Fig. 5 Histograms of sediment weight percentage measured from the samples taken at the beginning of the experiment (initial composition, black), and taken after each run from the sediment trap (trap) and the middle of the flume (bed)
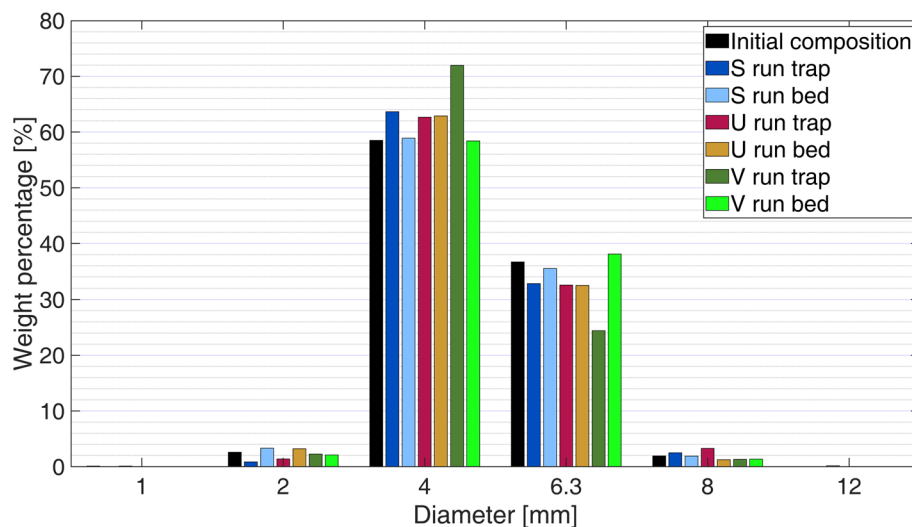
Velocity measurements

Regardless of the scenario, the bulk streamwise velocity U_P, calculated from the measured discharge and cross section area, varied between 0.84 and 0.86 m s^{-1} during the plateau (Table 4). The wave celerity was lower, the first wave being the slowest (0.44 m s^{-1}, Table 4).

The results obtained from the ADV refer to the point 2 cm above the bed. During the base flow, the velocity at this height was always around 0.34 m s^{-1} for all the runs, while there was a high difference between the ADV velocities measured during the wave plateau between runs U (0.45 m s^{-1}) and V (0.57 m s^{-1}). The mean vertical velocity registered by the ADV was the highest in the case of V (-0.011 m s^{-1}), while, for the other two cases, it was non-significant (Table 4).

In general, the MHD probe showed 0.10 m s^{-1} higher mean streamwise velocities than ADV, but for case U (Table 4). Higher values were recorded due to the higher probe position, which is a valid result according to the log law of velocity profile.

Bed surface changes for DCRP

The acquisition of digital images before and after each run permitted an evaluation of the bed changes due to the passage of the wave, via the comparison of the respective DSM, which resulted in differential models for each case (Fig. 6).

After the S run, characterized by the smallest flood wave, it is possible to observe a generalized erosion along the whole flume (Fig. 6a). The wave generated an erosion in the order of 3–10 mm, with a maximum deepening of around 12 mm, and there were a few accumulation areas, where the bed has been raised by 1–4 mm.

A similar behaviour appeared also for the intermediate run U (Fig. 6b). Here, the flume was affected by a generalized erosion of 1–12 mm, and a few areas presented a more significant deepening, reaching around 12–15 mm. In this

Table 4 Velocity measurements

Run	U_P (m s^{-1})	ADV U_P (m s^{-1})	MHD U_P (m s^{-1})	ADV W_P (m s^{-1})	$\tau_{adv,p}$ (N m^{-2})	C (m s^{-1})
S	0.86	0.44	0.54	-0.0002	1.32	0.44
U	0.86	0.45	0.59	-0.0017	1.57	0.62
V	0.84	0.57	0.67	-0.011	2.07	0.64

U_P—mean streamwise velocity during the wave plateau calculated from discharge and flow cross section area averaged between locations No. 1 and 4 ($U = Q/A$); $ADV\ U_P$—mean streamwise velocity measured by ADV probe during the wave plateau; $MHD\ U_P$—mean streamwise velocity measured by MHD probe during the wave plateau; $ADV\ W_P$—mean vertical velocity measured by ADV probe during the wave plateau; $\tau_{adv,p}$—Reynolds stress calculated from ADV records for the plateau (N m^{-2}); C—wave celerity
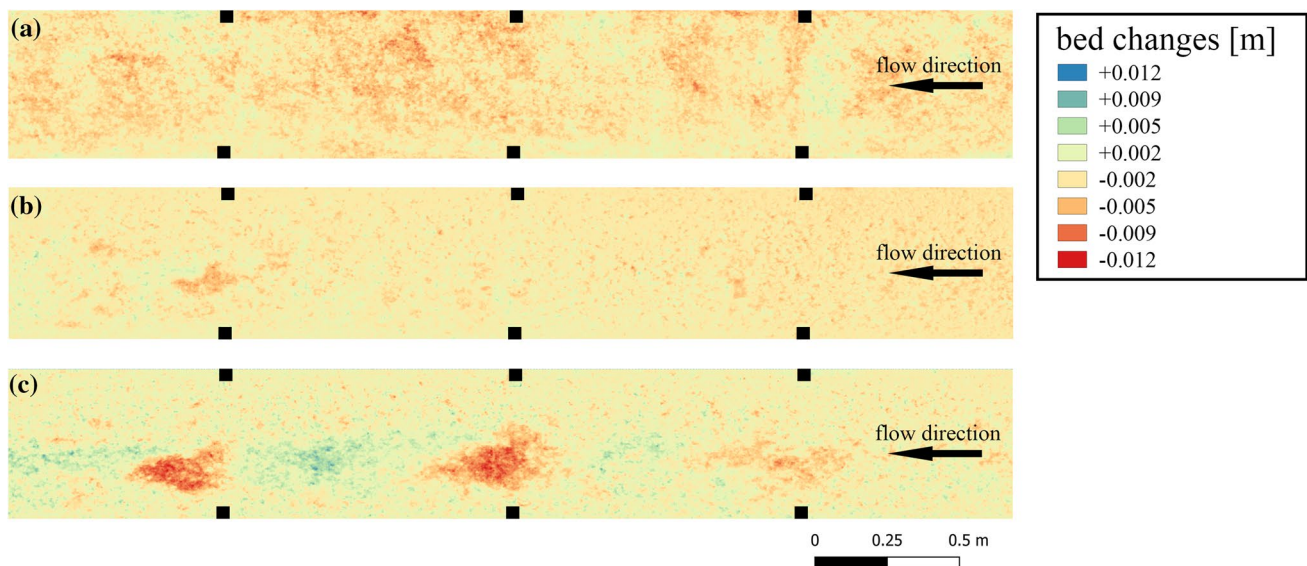

Fig. 6 Bed changes derived from DCRP: **a** run S; **b** run U; **c** run V. Erosion is represented in red, while deposition in blue. Control points and checkpoints are also indicated (see Fig. 2)

case, the wave passage caused local accumulations of around 2–4 mm, as pointed out by the green areas in the differential model (Fig. 6b).

As expected, the higher the flood wave, the more significant the bed changes (Fig. 6c). In run V, three large erosion areas (coloured in red) were observed, being around 30–50 cm long and 20–25 cm wide. In these regions, the bed has been lowered by 7–16 mm. By contrast, also three major accumulation areas were observed, but here the deposits reached only 2–10 mm.

Discussion

Effect of wave characteristics on bedload transport

The dimensionless bedload W_T^* was plotted against two unsteadiness parameters Γ_{HG} and ascension unsteadiness P_{gt} and total flow work index W_k (Fig. 7). As visible, the Γ_{HG} unsteadiness parameter shows a much more linear correlation with the dimensionless bedload W_T^* than the P_{gt}. One of the reasons for the different behaviour could be associated with the fact that, for computing Γ_{HG}, only the wave height-to-time ratio was taken into consideration, and this ratio changed at each run, decreasing as the wave magnitude increased. It is worth noting that if not the mean height was used, but rather the height where the waves were flattened, the Γ_{HG} parameter would be smaller. On the other hand, the ascension unsteadiness P_{gt} relies on two changing variables, namely the time of the rising limb and the peak flow velocity. Therefore, it reflects only the beginning of the wave, while the total bedload covers the sediment gathered in the trap until the wave passed. Consequently, the P_{gt} showed to be the least correlated parameter to W_T^* in comparison with the results in Bombar et al. (2011). In their experimental study, one run showed $P_{gt} = 0.0038$ and $W_k = 3.0$ for $W_T^* = 87.8$, while in our case $P_{gt} = 0.0015$ and $W_k = 2.7$ for $W_T^* = 85.9$. Aside from the

Fig. 7 Dimensionless bedload W_{t*} versus unsteadiness parameters Γ_{HG} and P_{gt}, as well as total water work W_k for the three scenarios

uncertainty correlated with the computation of the two unsteadiness parameters, the total flow work index may be used as a good coefficient to predict the total bedload. The correlation between W_T^* and Γ_{HG} or W_k obtained during our experiments agreed with the study of Bombar et al. (2011), as visible in Fig. 7. That said, the trapezoidal wave magnitude and its flashiness have an impact on bedload consistent with the literature (Bombar et al. 2011), even if they analysed proper triangular waves.

In the considered case, computing the water surface slope (Eq. 6) and hence the bed shear stress using the Saint-Venant model for a diffusive wave (Eq. 5) was problematic during both the rising and falling limbs of the flood wave, as the differences between consecutive water levels were significant for calculations. In specifics, in calculations of $\tau_{b,p}$, water depth h was a mean of depth at points S1 and S4, which gave us perspective on the mean conditions between those two points, which was needed to compare results to the ADV, placed roughly in the middle of this flume section (Fig. 1). In reality, conditions between points S1 and S4 were not the same. The wave height at the point 3.6 m (S4, Fig. 1) from the outlet reached 0.020 m less than in the point at the middle of the channel length (S1, Fig. 1) in run S. For run U, it was 0.037 m, and only for the last run V, the wave was visible along the flume, as the difference in ΔH between the points was 0.002 m.

The preservation of the wave shape along the flume in run V was coupled with the double peak in q during the plateau. In this case, T_{lag}, considering the moment of the higher peak, reached 20% of the rising time, in comparison with 22% in run U and 10% reported by Bombar et al. (2011), though their experiments were conducted with a 0.005 flume slope.

The transported sediment composition showed a bigger volume of gravel fraction moved by the V wave in comparison with S and U waves (Fig. 5). This result translated into characteristic grain size is consistent with Wang et al. (2015), who observed that, generally, the D_{50} from the trap was lower than from the bed samples. However, increasing the duration of the wave could reshape transported sediment distribution, as it tends to be better sorted and finer with the passing time (McLaren and Bowles 1985).

Boundary Reynolds number is a suitable parameter for characterising bedload transport of sand, which usually occurs in the lower Re^* range, namely for $Re^* < 400$ (i.e. Török et al. 2019), in which range our experiments were placed. The comparison of the boundary Reynolds number Re_p^* and Shields stress $\tau_{*,p}$ (Table 2) with the Shields's curve showed that, for the run S, sediment transport should not occur, though almost 0.2 kg of the sediment was found in the trap. In that regard, using the values of bed shear
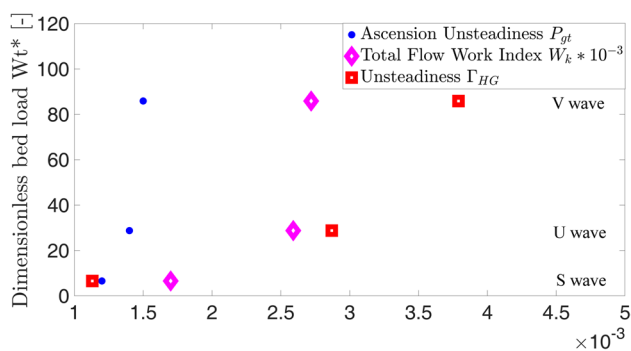
extrapolated from ADV measurements would not change the view on the Shields curve, as $\tau_{\text{BedAdv,p}}$ was lower than $\tau_{\text{b,p}}$ in every scenario. On the other hand, shear velocity derived from ADV (Table 2) is more correlated with measured dimensionless bedload W_T^* (Table 1). Regarding more on the usability of ADV measurements, in run *V*, both the recorded streamwise and vertical velocity fluctuations were the highest among all the scenarios, resulting in the highest $\tau_{\text{adv,p}}$ Reynolds stress (2.07 N m^{-2}) among all scenarios (Table 4). In summary, the differences in Reynolds stress and bedload transport between runs were not correlated, which is in line with the work of Yager et al. (2018).

Accuracy of DCRP

Digital image processing, 3D modelling and point cloud generation entail certain errors that may affect the quality of images and, consequently, the accuracy of the measurement. First, a major element influencing the accuracy is the quality of the digital camera. To correctly obtain the perspective projection performed with the camera, it is necessary to determine intrinsic camera parameters, namely the focal length and the position of the principal point in an image sensor, as well as estimating the radial and tangential lens distortions (Cronk et al. 2006; Luhmann et al. 2016; Wójcik et al., 2018).

An equally important element is the image ground sample distance (GSD), which defines the achievable accuracy of tie points between images from which relative orientation can be estimated. Moreover, it determines the accuracy of indication GCP having coordinates in a given reference system. The accuracy of the estimated absolute orientation elements of the entire block of photos depends on the errors contained in the GCP indication in the individual images, as well as on the mean error for the entire geometric system. In the case of establishing a sufficiently large number of GCP for a block of photos, it is possible to treat the internal orientation elements of the photos and distortion parameters as unknowns and then determine them in a common calculation process, together with the external orientation elements of the photos, implemented by the bundle adjustment algorithm (Luhmann et al. 2019).

The precision of our photogrammetric study, in terms of RMSE of control and checkpoints, is presented in Table 5. They can be considered satisfactory, in particular considering the RMSE for the vertical (*Z*) coordinate on the ChP (checkpoints), which was, on average, 1.9 mm, with a maximum value of 2.6 mm. Lower accuracies were obtained for the *X* and *Y* positions of the ChP, with an average RMSE of 6.9 mm and 6.0 mm for the *X* and *Y* coordinates, respectively. These values were mostly due to the quality of the measuring equipment used in our experiments, as well as the unfavourable geometry of control and checkpoints. Therefore, to obtain more reliable results, an update of the instrumentations is needed.

Conclusions

With a relatively simple experimental set-up, we confirmed that the bedload transport rate is mainly a function of the flood magnitude. But, besides the flood magnitude, the flow unsteadiness is the most significant parameter that triggers erosion and deposition phenomena. However, in the presence of backwater, no discernible bed structures were visible during the wave passage.

Table 5 Positioning error of control points (CP) and checkpoints (ChP), before and after each run

Test	X error (m)	Y error (m)	Z error (m)	Total error (m)	Reprojection error (pix)
S, CP, before	0.0065	0.0078	0.0015	0.0103	0.16
S, ChP, before	0.0067	0.0052	0.0019	0.0087	0.22
S, CP, after	0.0081	0.0062	0.0020	0.0104	0.09
S, ChP, after	0.0046	0.0052	0.0014	0.0071	0.12
U, CP, before	0.0092	0.0058	0.0009	0.0109	0.17
U, ChP, before	0.0050	0.0066	0.0013	0.0084	0.11
U, CP, after	0.0053	0.0073	0.0015	0.0092	0.46
U, ChP, after	0.0076	0.0060	0.0024	0.0100	0.36
V, CP, before	0.0074	0.0040	0.0016	0.0086	0.09
V, ChP, before	0.0093	0.0042	0.0026	0.0106	0.18
V, CP, after	0.0081	0.0059	0.0017	0.0101	0.39
V, ChP, after	0.0081	0.0089	0.0016	0.0121	0.62
RMSECP	0.0074	0.0062	0.0015	0.0099	0.23
RMSE ChP	0.0069	0.0060	0.0019	0.0095	0.27

The three trapezoidal flood waves, with increasing flashiness, were tested: S, U and V. The water level was more uneven along the flume during the wave passage for cases S and U than for case V, which was especially visible from the middle towards the end of flume sections. This caused a weak correlation of the bedload with the wave ascension unsteadiness (P_{gt}), but the wave flashiness parameter (Γ_{HG}) retained almost linear correlation. In other words, the flattening of the wave near the end of the flume affected the amount of water acting on the bed (W_k) for cases S and U. Therefore, there was a big jump in the amount of material weighted in the trap (W_T^*) in comparison with the wave V. Despite the Shields curve showing that there should be no motion of the sediment during the S wave, smaller fractions were still transported and captured by the sediment trap. That highlights problems in calculating the bulk bed shear stress and correlated sediment transport in non-uniform flow conditions. Comparing our results with literature evidence (Bombar et al. 2011), the lag time T_{lag} seems to increase due to zero-slope conditions.

The bedload transport under unsteady flow conditions is a complex issue. In the present work, only preliminary experiments on trapezoidal-shaped waves were carried out, but far more problems should be explored in the future. We found that the wave having the higher magnitude caused an 8-shaped hysteresis curve, while the lower waves did not show specific behaviours. However, in the present work, only the passage of a single trapezoidal wave was considered, while real-world streams have more complex hydrology, due to a combination of natural flow variability and anthropogenic pressure. Observing the results shown in Fig. 3, it can be stated that flow conditions with zero bed slope caused rapid changes in sediment transport, which vanished just after the falling limb of the wave appeared. This phenomenon was observable for all the presented waves (S, U, V). In other words, for the zero bed slope conditions, the maximal sediment flux depended on the amount of flowing water as well as on the exceeding limit of the critical stresses for incipient motion. However, the transport subsided at the start of wave decrease, earlier than at the moment when the stresses become lower than critical.

In nature, river flows are driven by gravity, and bed slope has a high influence on bedload transport. The zero-slope case is limited to some specific yet important local situations, e.g. flow affected by hydraulic structures. Therefore, using a zero-slope flume to model processes in a river is an oversimplification that should be addressed in the future, performing additional experiments that consider a larger range of slopes.

Declarations

Conflict of interest All authors declare that there is no conflict of interest.

Ethical approval This paper does not contain any studies with human participants or animals performed by any of the authors.

References

Abderrezzak KEK, Paquier A, Gay B (2008) One-dimensional numerical modelling of dam-break waves over movable beds: application to experimental and field cases. Environ Fluid Mech 8:169–198. https://doi.org/10.1007/s10652-008-9056-9

Aigner J, Kreisler A, Rindler R, Hauer C, Habersack H (2017) Bedload pulses in a hydropower affected alpine gravel bed river. Geomorphology 291:116–127. https://doi.org/10.1016/j.geomorph.2016.05.015

Bartnik W, Banasik K, Książek L, Radecki-Pawlik A, Strużynski A (2005) Forecasting of fluvial processes on the Skawa River within back-water reach of the Świnna Poręba water reservoir. Publ Inst Geophy Pol Acad Sci 5(387):57–85

Berta AM, Bianco G (2010) An expression for the water-sediment moving layer in unsteady flows valid for open channels and embankments. Nat Hazards Earth Syst 10(5):1051–1059. https://doi.org/10.5194/nhess-10-1051-2010

Bombar G, Elci S, Tayfur G, Guney S, Bor A (2011) Experimental and numerical investigation of bed-load transport under unsteady flows. J Hydraul Eng 137(10):1276–1282. https://doi.org/10.1061/(ASCE)HY.1943-7900.0000412

Bracken LJ, Turnbull L, Wainwright J, Bogaart P (2015) Sediment connectivity: a framework for understanding sediment transfer at multiple scales. Earth Surf Proc Land 40(2):177–188. https://doi.org/10.1002/esp.3635

Cronk S, Fraser CS, Hanley HB (2006) Automatic calibration of colour digital cameras. Photogramm Rec 21(116):355–372. https://doi.org/10.1111/j.1477-9730.2006.00380.x

Faezal N, Mohd F, Nurul L, Radzuan S, Zulkiflee I, Mushairry M, Muhammad A (2016) Monitoring laboratory scale river channel profile changes using digital close range photogrammetry technique. Malays J Civ Eng 28(3):252–266. https://doi.org/10.11113/mjce.v28.16012

Goring DG, Nikora VI (2002) Despiking acoustic Doppler velocimeter data. J Hydraul Eng 128(1):117–126. https://doi.org/10.1061/(ASCE)0733-9429(2002)128:1(117)

Graf WH, Suszka L (1985) Unsteady flow and its effect on sediment transport. In: Proceedings of the 21st IAHR congress, pp 1–5

Guney MS, Bombar G, Aksoy AO (2013) Experimental study of the coarse surface development effect on the bimodal bed-load transport under unsteady flow conditions. J Hydraul Eng 139(1):12–21. https://doi.org/10.1061/(ASCE)HY.1943-7900.0000640

Hitchcock JN (2020) Storm events as key moments of microplastic contamination in aquatic ecosystems. Sci Total Environ 734:139436. https://doi.org/10.1016/j.scitotenv.2020.139436

Humphries R, Venditti JG, Sklar LS, Wooster JK (2012) Experimental evidence for the effect of hydrographs on sediment pulse dynamics in gravel-bedded rivers. Water Resour Res 48:W01533. https://doi.org/10.1029/2011WR010419

Jin ZW, Lu JY, Wu HL (2016) Study of bedload transport in backwater flow. J Hydrodyn 28(1):153–161. https://doi.org/10.1016/S1001-6058(16)60616-9

Książek L, Woś A, Florek J, Wyrębek M, Młyński D, Wałęga A (2019) Combined use of the hydraulic and hydrological methods to calculate the environmental flow: Wisłoka river, Poland: case study. Environ Monit Assess 191(254):1–17. https://doi.org/10.1007/s10661-019-7402-7

Książek L, Mitka B, Mrokowska M, Nones M, Phan CN, Przyborowski Ł, Strużyński A, Wojak S, Wyrębek M (2021) Application of digital close-range photogrammetry to determine changes in gravel bed surface due to transient flow conditions. Publ Inst Geophys Pol Acad Sci 434((E-11)):95–96. https://doi.org/10.25171/InstGeoph_PAS_Publs-2021-028

Książek L, Woś A, Wyrębek M, Strużyński A (2020) Habitat structure changes of the Wisłoka River as a result of channel restoration. In: Kalinowska M, Mrokowska M, Rowiński P (eds) Recent trends in environmental hydraulics. GeoPlanet: Earth and planetary sciences. Springer Nature, Basel, pp 103–115. https://doi.org/10.1007/978-3-030-37105-0_9

Lee H, Balachandar S (2012) Critical shear stress for incipient motion of a particle on a rough bed. J Geophys Res Earth 117:1026. https://doi.org/10.1029/2011JF002208

Li ZJ, Qian HL, Cao ZX, Liu HH, Pender G, Hu PH (2018) Enhanced bed load sediment transport by unsteady flows in a degrading channel. Int J Sediment Res 33:327–339. https://doi.org/10.1016/j.ijsrc.2018.03.002

Luhmann T, Fraser C, Maas HG (2016) Sensor modelling and camera calibration for close-range photogrammetry. ISPRS J Photogramm 115:37–46. https://doi.org/10.1016/j.isprsjprs.2015.10.006

Luhmann T, Robson R, Kyle S, Boehm J (2019) Close-range photogrammetry and 3D imaging, 3rd edn. De Gruyter, Berlin. https://doi.org/10.1515/9783110607253

Luo X, Yang S, Zhang J (2012) The impact of the Three gorges dam on the downstream distribution and texture of sediments along the middle and lower Yangtze river (Changjiang) and its estuary, and subsequent sediment dispersal in the east China sea. Geomorphology 179:126–140. https://doi.org/10.1016/j.geomorph.2012.05.034

Manes C, Pokrajac D, McEwan I (2007) Double-averaged open-channel flows with small relative submergence. J Hydraul Eng 133(8):896–904. https://doi.org/10.1061/(ASCE)0733-9429(2007)133:8(896)

Mao L (2012) The effect of hydrographs on bed load transport and bed sediment spatial arrangement. J Geophys Res 117:F03024. https://doi.org/10.1029/2012JF002428

Maselli V, Normandeau A, Nones M, Tesi T, Langone L, Trincardi F, Bohacs KM (2020) Tidal modulation of river-flood deposits: How low can you go? Geology 48(7):663–667. https://doi.org/10.1130/G47451.1

McLaren P, Bowles D (1985) The effects of sediment transport on grain-size distributions. J Sediment Res 55(4):457–470

Michalik A, Książek L (2009) Dynamics of water flow on degraded sectors of polish mountain stream channels. Pol J Environ Stud 18(4):665–672

Mikrut S (2009) Przydatność algorytmów podpikselowej detekcji cech w wybranych zagadnieniach fotogrametrycznych. Archiwum Fotogrametrii, Kartografii i Teledetekcji 19:299–308 (**in Polish**)

Mitka B, Pluta M (2016) Comparative analysis of the process of creating a 3D model of architecture object with using laser scanning and structure from motion technologies. In: 16th international multidisciplinary scientific GeoConference. SGEM 2. Curran Associates, Inc, pp 847–854

Mrokowska MM, Rowiński PM (2019) Impact of unsteady flow events on bedload transport: a review of laboratory experiments. Water 11(5):907. https://doi.org/10.3390/w11050907

Mrokowska MM, Rowiński PM, Książek L, Strużyński A, Wyrębek M, Radecki-Pawlik A (2018) Laboratory studies on bedload transport under unsteady flow conditions. J Hydrol Hydromech 66(1):23–31. https://doi.org/10.1515/johh-2017-0032

Mrokowska MM, Rowiński PM, Książek L, Strużyński A, Wyrębek M, Radecki-Pawlik A (2016) Flume experiments on gravel bed load transport in unsteady flow—preliminary results. In: Rowiński P, Marion A (eds) Hydrodynamic and mass transport at freshwater aquatic interfaces. Geoplanet Earth and planetary sciences. Springer, Berlin, pp 221–233. https://doi.org/10.1007/978-319-27750-9_18

Nones M, Varrani A, Franzoia M, Di Silvio G (2019) Assessing quasi-equilibrium fining and concavity of present rivers: a modelling approach. CATENA 181:104073. https://doi.org/10.1016/j.catena.2019.104073

Parsheh M, Sotiropoulos F, Porte-Agel F (2010) Estimation of power spectra of acoustic-Doppler velocimetry data contaminated with intermittent spikes. J Hydraul Eng 136(6):368–378. https://doi.org/10.1061/(ASCE)HY.1943-7900.0000202

Phillips CB, Hill KM, Paola C, Singer MB, Jerolmack DJ (2018) Effect of flood hydrograph duration, magnitude, and shape on bed load transport dynamics. Geophys Res Lett 45(16):8264–8271. https://doi.org/10.1029/2018GL078976

Plumb BD, Juez C, Annable WK, McKie CW, Franca MJ (2020) The impact of hydrograph variability and frequency on sediment transport dynamics in a gravel-bed flume. Earth Surf Proc Land 45:816–830. https://doi.org/10.1002/esp.4770

Przyborowski Ł, Nones M, Mrokowska M, Książek L, Phan CN, Strużyński A, Wyrebek M (2021) Laboratory Investigation of sediment transport under transient flow—preliminary results. Publ Inst Geophys Pol Acad Sci 434((E-11)):75–76. https://doi.org/10.25171/InstGeoph_PAS_Publs-2021-023

Redolfi M, Bertoldi W, Tubino M, Welber M (2018) Bed load variability and morphology of gravel bed rivers subject to unsteady flow: a laboratory investigation. Water Resour Res 54:842–862. https://doi.org/10.1002/2017WR021143

Savitzky A, Golay MJ (1964) Smoothing and differentiation of data by simplified least squares procedures. Anal Chem 36(8):1627–1639

Stojic M, Chandler J, Ashmore P, Luce J (1998) The assessment of sediment transport rates by automated digital photogrammetry. Photogramm Eng Rem S 64(5):387–395

Török GT, Józsa J, Baranya S (2019) A shear Reynolds number-based classification method of the nonuniform bed load transport. Water 11(1):73. https://doi.org/10.3390/w11010073

Wahl TL (2003) Discussion of 'despiking acoustic Doppler velocimeter data' by Derek G. Goring and vladimir I. Nikora J Hydraul Eng 129:484–487. https://doi.org/10.1061/(ASCE)0733-9429(2003)129:6(484)

Wang L, Cuthbertson AJS, Pender G, Cao Z (2015) Experimental investigations of graded sediment transport under unsteady flow hydrographs. Int J Sediment Res 30:306–320. https://doi.org/10.1016/j.ijsrc.2015.03.010

Wang L, Cuthbertson A, Pender G, Zhong DY (2019) Bed load sediment transport and morphological evolution in a degrading uniform sediment channel under unsteady flow hydrographs. Water

Resour Res 55:431–5452. https://doi.org/10.1029/2018WR024413

Wang L, Cuthbertson AJ, Zhang SH, Pender G, Shu AP, Wang YQ (2021) Graded bed load transport in sediment supply limited channels under unsteady flow hydrographs. J Hydrol 595:126015. https://doi.org/10.1016/j.jhydrol.2021.126015

Waters KA, Curran JC (2015) Linking bed morphology changes of two sediment mixtures to sediment transport predictions in unsteady flows. Water Resour Res 51:2724–2741. https://doi.org/10.1002/2014WR016083

Wójcik A, Klapa P, Mitka B, Sładek J (2018) The use of the photogrammetric method for measurement of the repose angle of granular materials. Measurement 115:19–26. https://doi.org/10.1016/j.measurement.2017.10.005

Wu C, Nitterour JA (2020) Impacts of backwater hydrodynamics on fluvial–deltaic stratigraphy. Basin Res 32(3):567–584. https://doi.org/10.1111/bre.12385

Yager EM, Venditti JG, Smith HJ, Schmeeckle MW (2018) The trouble with shear stress. Geomorphology 323:41–50. https://doi.org/10.1016/j.geomorph.2018.09.008

Yen CL, Lee KT (1995) Bed topography and sediment sorting in channel bend with unsteady flow. J Hydraul Eng 121(8):591–599. https://doi.org/10.1061/(ASCE)0733-9429(1995)121:8(591)